Integration of GOCI and AHI Yonsei Aerosol Optical Depth Products During the 2016 KORUS-AQ and 2018 EMeRGe Campaigns

Hyunkwang Lim[1], Sujung Go[1,2], Jhoon Kim[1], Myungje Choi[2,3], Seoyoung Lee[1], Chang-Keun Song[4], Yasuko Kasai[5]

[1]Department of Atmospheric Sciences, Yonsei University, Seoul 03722, Republic of Korea
[2]Joint Center for Earth Systems Technology, University of Maryland Baltimore County, Baltimore, MD, USA
[3]Jet Propulsion Laboratory, California Institute of Technology, Pasadena, CA, USA
[4]School of Urban and Environmental Engineering, Ulsan National Institute of Science and Technology, Ulsan 44919, Republic of Korea
[5]Natinal Institute of Information and Communications Technology, Tokyo 184-8759, Japan

Correspondence to: Jhoon Kim (jkim2@yonsei.ac.kr)

Abstract. The Yonsei AErosol Retrieval (YAER) algorithm for the Geostationary Ocean Color Imager (GOCI) retrieves aerosol optical properties only over dark surfaces, so it is important to mask pixels with bright surfaces. The Advanced Himawari Imager (AHI) is equipped with three shortwave-infrared and nine infrared channels, which is advantageous for bright-pixel masking. In addition, multiple visible and near-infrared channels provide a great advantage in aerosol property retrieval from the AHI and GOCI. By applying the YAER algorithm to 10 minute AHI or 1 hour GOCI data at 6 km × 6 km resolution, diurnal variations and aerosol transport can be observed, which has not previously been possible from low-earth-orbit satellites. This study attempted to estimate the optimal aerosol optical depth (AOD) for East Asia by data fusion, taking into account satellite retrieval uncertainty. The data fusion involved two steps: (1) analysis of error characteristics of each retrieved result with respect to the ground-based Aerosol Robotic Network (AERONET), and bias correction based on normalized difference vegetation indexes; and (2) compilation of the fused product using ensemble-mean and maximum-likelihood estimation methods (MLE). Fused results show a better statistics in terms of fraction within the expected error, correlation coefficient, root-mean-square error, median bias error than the retrieved result for each product. If the root mean square error and mean AOD bias~~Gaussian center~~ values used for MLE fusion are correct, the MLE fused products show better accuracy, but the ensemble-mean products can still be used as useful as MLE.

1. Introduction

Aerosols are generated by human activities and natural processes on local to global scales, and have a lifetime of several to tens of days. Aerosols affect Earth's radiative energy balance by scattering and absorption (e.g. Cho et al., 2003). High aerosol loadings are persistent in Northeast Asia, including diverse aerosol types from various sources. Interactions among aerosols, clouds, and radiation in the atmosphere cause significant uncertainties in climate-model calculations (IPCC, 2013). Datasets produced by satellites have been widely used to reduce such uncertainties (Saide et al., 2014; Pang et al., 2018), but the systems must be

43   accurately calibrated, verified, and consistent. Satellite data have been used extensively to
44   retrieve aerosol optical properties (AOPs) over broad areas, with several algorithms having
45   been developed. Satellites in low earth orbit (LEO), including Sun-synchronous orbit (SSO),
46   cover the entire Earth over one to several days, depending on instrument and orbit
47   characteristics. Most aerosol retrieval algorithms have been developed for LEO satellites
48   (Kim et al., 2007; Lyapustin et al., 2011a, b; Lee et al., 2012; Fukuda et al., 2013; Hsu et al.,
49   2013; Levy et al., 2013; Garay et al., 2017, 2020). LEO instruments currently onboard
50   satellites include the Moderate Resolution Imaging Spectrometer (MODIS), Visible Infrared
51   Imaging Radiometer Suite (VIIRS), Multi-angle Imaging SpectroRadiometer (MISR), and
52   Cloud and Aerosol Imager (CAI) (Remer et al., 2005; Lyapustin et al., 2011a, b, 2018;
53   Fukuda et al., 2013; Hsu et al., 2013; Levy et al., 2013; Garay et al., 2017, 2020; Jackson et
54   al., 2013; Lee et al., 2017).
55   Representative algorithms developed for MODIS data include the Dark-Target (DT; Remer
56   et al., 2005; Levy et al., 2013), Deep Blue (DB; Hsu et al., 2013; Sayer et al., 2014), and
57   Multi-Angle Implementation of Atmospheric Correction (MAIAC; Lyapustin et al., 2011a, b)
58   systems, which are also applied for the succeeding VIIRS (Sayer et al., 2018). In the DT
59   algorithm, the 2.1 μm channel is used to estimate land-surface reflectance in the visible (VIS)
60   region using empirical equations based on the normalized difference vegetation index
61   (NDVI). The DT algorithm has improved surface-reflectance modelling through
62   consideration of the fractional area of urbanization (Gupta et al., 2016). Ocean-surface
63   reflectance is estimated using the Cox and Munk method (Cox and Munk, 1954), and AOPs
64   over land and ocean are provided at spatial resolutions of 10 km × 10 km and 3 km × 3 km
65   (Remer et al., 2013), respectively. The DB algorithm has an advantage over the DT algorithm
66   in allowing aerosol data retrieval over bright surfaces. By using a shorter-wavelength channel,
67   accuracy is improved over bright surfaces such as urban and desert areas, where surface
68   reflectance was previously estimated by the minimum reflectance method (MRM; Herman
69   and Celarier 1997; Koelemeijer et al., 2003; Hsu et al., 2004). Furthermore, with the
70   improvement to Collection 6.1, land-surface reflectance can be estimated similarly to the DT
71   method, over densely vegetated regions (Sayer et al., 2019). In the case of VIIRS DB, aerosol
72   retrieval over the ocean is also applied by the Satellite Ocean Aerosol Retrieval (SOAR)
73   algorithm (Sayer et al., 2018). In the MODIS MAIAC system, surface reflectance is
74   estimated by considering various images based on time-series analysis, with multi-angle
75   observations, based on up to 16 day data, and by applying the bidirectional reflectance
76   distribution function (BRDF). Ocean-surface reflectance is determined using a Cox and
77   Munk BRDF model similar to DT and VIIRS DB (Lyapustin et al., 2011a, b, 2018). The
78   MISR observes Earth at nine different angles, providing a high degree of freedom for signals;
79   consequently, retrievals yield estimates of aerosol type and shape. As with the MAIAC,
80   multiple observations are used, with the estimation of land-surface reflectance involving
81   bidirectional reflectance factors (BRF). Zhang et al. (2016) developed an aerosol retrieval
82   algorithm that allows aerosol data retrieval over bright land surfaces using surface-reflectance
83   ratios from the VIIRS.
84   Aerosol retrieval algorithms for geosynchronous Earth orbit (GEO) satellites have been
85   developed, including the Geostationary Operational Environmental Satellite (GOES) series in
86   the USA (Knapp et al., 2005), Meteosat series in Europe (Bernard et al., 2011), Himawari
87   series in Japan (Yoon et al., 2007; Kim et al., 2008; Lim et al., 2018; Kikuchi et al., 2018;
88   Yoshida et al., 2018; Gupta et al., 2019), and the Geostationary Korea Multi-Purpose Satellite
89   (GEO-KOMPSAT, GK) series in South Korea (Kim et al., 2014, 2016; Choi et al., 2016,
90   2018; Kim et al., 2020). However, previously launched geostationary meteorological
91   satellites had only a single, broadband VIS channel, with which it is difficult to retrieve

92   AOPs other than aerosol optical depth (AOD) (Wang et al., 2003; Knapp et al., 2005; Kim et
93   al., 2008, 2014, 2016; Bernard et al., 2011). However, the Geostationary Ocean Color Imager
94   (GOCI) onboard the GK-1 satellite, also known as the Communication, Ocean, and
95   Meteorological Satellite (COMS), has six VIS and two near-infrared (NIR) channels, which
96   is advantageous for retrieving AOPs (Lee et al., 2010; Choi et al., 2016, 2018; Kim et al.,
97   2017). Next-generation meteorological GEO satellite instruments, including the Advanced
98   Himawari Imager (AHI), Advanced Baseline Imager (ABI), and Advanced Meteorological
99   Imager (AMI), have three to four VIS and NIR channels, which enable aerosol property
100 retrieval with high accuracy (Lim et al., 2016, 2018; Kikuchi et al., 2018; Yoshida et al.,
101 2018; Gupta et al., 2019). Kikuchi et al. (2018) and Yoshida et al. (2018) performed aerosol
102 retrievals using the MRM and corrected reflectance using empirical equations. Gupta et al.
103 (2019) extended the MODIS DT algorithm to GEO satellites and estimated visible surface
104 reflectance using SWIR reflectance. Lim et al. (2018) retrieved the AOPs using both MRM
105 and estimated surface reflectance from short-wave IR (SWIR) data (ESR), and presented the
106 two merged products: an L2-AOD merged product, and a reprocessed AOD produced by
107 merging MRM and ESR surface reflectances. The MRM gives better accuracy over brighter
108 surfaces such as urban areas, while the ESR method gives better accuracy over areas of dense
109 vegetation (Lim et al., 2018). However, there is a critical surface reflectance at which aerosol
110 signals disappear, depending on the single-scattering albedo (Kim et al., 2016). Over the
111 ocean, both the MRM and ESR methods give high accuracy, but ESR results are robust with
112 the Cox and Munk model.
113 The MRM requires more computational time than the ESR method to estimate surface
114 reflectance, as it requires data for the past 30 days, and LER needs to be calculated using a
115 radiative transfer model. The ESR method estimates surface reflectance from the observed
116 TOA reflectance at 1.6 μm wavelength using empirical equations including the NDVI. The
117 advantage of MRM is that stable surface reflectance values can be obtained regardless of
118 surface type. However, due to the influence of background aerosol optical depth (BAOD),
119 surface reflectance tends to be overestimated, with satellite-derived AOD data thus being
120 underestimated (Kim et al., 2014). On the other hand, the ESR method uses TOA reflectance
121 at 1.6 μm wavelength to detect surface signals, which is less sensitive to fine particles and
122 BAOD. However, when aerosols such as yellow dust with coarse particles are transported
123 from the Taklamakan and Gobi deserts, the BAOD effect also applies to the ESR method.
124 The ESR method is also more likely to be affected by snow surfaces than the MRM, as snow
125 reduces reflectivity around the 1.6 μm wavelength (Negi and Kokhanovsky, 2011). The ESR
126 method also has the disadvantage of giving noisy results over bright surfaces such as desert.
127 However, its fast surface-reflectance estimation enables near-real-time retrieval based on the
128 AHI YAER algorithm.
129
130   Algorithms developed to date for LEO and GEO satellites have both advantages and
131 disadvantages, depending on algorithm characteristics. Therefore, the MODIS team provides
132 combined DT and DB AOD products (Levy et al., 2013; Sayer et al., 2014). In addition,
133 several studies of the fusion of L2 products have been conducted (Levy et al., 2013; Sayer et
134 al., 2014; Wei et al., 2019), with Bilal et al. (2017) obtaining reliable results from merged DT
135 and DB products, as indicated by the NDVI in East Asia, and also robust products by simply
136 averaging DT and DB without consideration of the NDVI.
137 AOP data fusion in East Asia may also be achieved using aerosol products of AMI, GOCI-2,
138 and the geostationary environment monitoring spectrometer (GEMS) onboard the GK-2A and
139 2B satellites launched by South Korea in 2018 and 2020, respectively, with accuracy over
140 bright surfaces being improved by the GEMS aerosol product. It is also possible to obtain

141 accurate AOPs ~~and aerosol-related variables,~~ such as single-scattering albedo, ~~aerosol loading~~
142 ~~height,~~ and fine-mode fraction, and aerosol loading height, which have been difficult to
143 obtain by fusion of L2 data and/or surface reflectance data. If the trace-gas dataset retrieved
144 from GEMS is used, it is possible to improve the aerosol type, with the retrieval of high-
145 quality AOD data (Go et al., 2020).
146   Several studies have considered AOD data fusion, for which methods can be broadly
147 classified into two types. First, the fusion of more than one AOD product may involve
148 optimal interpolation (Xue et al., 2012), linear or second-order polynomial functions (Mélin
149 et al., 2007), arithmetic or weighted means (Gupta et al., 2008), or maximum-likelihood
150 estimates (MLE) (Nirala, 2008; Xu et al., 2015; Xie et al., 2018). Second, in the absence of
151 satellite-derived AOD products for the day of fusion, the geostatistical fusion method,
152 universal kriging method (Chatterjee et al., 2010; Li et al., 2014), geostatistical inverse
153 modelling (Wang et al., 2013), or spatial statistical data fusion (Nguyen et al., 2012) may be
154 applied. These have the advantage that AOD can be estimated by integrating the spatial
155 autocorrelation of AOD data even for pixels missing from the AOD products, although there
156 is a disadvantage in not considering temporal correlations. The Bayesian maximum entropy
157 (BME) method, taking into account temporal autocorrelation, has also been developed (Tang
158 et al., 2016). BME methodology can estimate gap-filling pixels that are difficult to retrieve
159 due to clouds, but with somewhat reduced accuracy. Gap filled AOD using the BME method,
160 and satellite-derived AOD discontinuity arises from insufficient temporal sampling being
161 available with the use of LEO satellites, resulting in a low fusion synergy. Previous studies
162 mentioned above include data fusion based on Kriging, reproduction of spectral AOD, and
163 BME method. Most of them focus on gap filling and rebuild AOD in areas not observed by
164 MISR, MODIS, and SeaWiFS, and so on (Wang et al., 2013; Tang et al., 2016). However in
165 this study, we focused on optimized AOD products with improved accuracy at the retrieved
166 pixels by ensemble-mean and MLE fusion. We compared these two products, one very
167 simple one and the other with more elaborated processes. As previous AOD fusion studies
168 improved the retrieved results mainly based on MLE or NDVI-based fusion studies (Bilal et
169 al., 2017; Levy et al., 2013; Wei et al., 2019; Go et al., 2020), we tried to further improve
170 them with efficient approach to save computation time considering the nature of satellite data
171 file size and user's near-real-time demand for data assimilation.
172 In this study, the GEO satellite dataset was used to resolve the temporal sampling issue for
173 data fusion, while maintaining the spatio-temporal resolution retrieved from GEO satellites.
174 We also attempted to estimate fused AOD products at 550nm with higher accuracy in East
175 Asia. The ensemble-mean and MLE methods were applied. Section 2 describes the two
176 algorithms used in this study for AHI and GOCI. Section 3 mentions methods of fusion and
177 systematic bias correction, and section 4 performs validation of the fused products with the
178 Aerosol Robotic Network (AERONET) instruments during two field campaigns: the Korea–
179 United States Air Quality Study (KORUS-AQ) and the Effect of Megacities on the Transport
180 and Transformation of Pollutants on Regional and Global Scales Study (EMeRGe).

181 **2. Descriptions of AHI, GOCI, the YAER algorithm**

182 **2.1 AHI aerosol algorithm**

183   The Himawari-8 and -9 satellites were launched by the Japanese Meteorological Agency
184 (JMA) on 7 October 2014 and 2 November 2016, respectively. The AHI onboard these
185 satellites has 16 channels covering wavelengths of 0.47–13.3 μm and performs full-disk and
186 Japan-area observations every 10 and 2.5 min, respectively, from GEO at 140.7° E longitude

187 (Bessho et al., 2016). Visible and NIR observations are also performed at high spatial
188 resolutions of 0.5–1.0 km, with SWIR to IR at 2 km, which have advantages in aerosol
189 property retrieval and cloud masking.
190 Lim et al. (2018) developed the AHI Yonsei aerosol retrieval (YAER) algorithm and
191 provided two retrieval results with 6 km × 6 km resolution based on MRM and ESR using
192 SWIR data. Aerosol property retrieval using VIS channels requires accurate surface
193 reflectance, for which MRM and ESR are useful, with the main difference between the two
194 lying in the surface-reflectance estimation method.
195   The MRM applies the minimum-reflectance technique over both land and ocean (Lim et al.,
196 2018), with surface reflectance being estimated by finding the minimum reflectance in each
197 pixel over the past 30 day window, giving the Lambertian equivalent reflectance (LER; Kim
198 et al., 2016; Lim et al., 2018). This method takes the bidirectional characteristics of surface
199 reflectance into consideration by obtaining surface reflectance at each observation time over
200 the 30-day search window. However, the method assumes that there is more than one clear
201 day during the search window and that surface reflectance does not change; otherwise, it is
202 affected by clouds and/or the BAOD (Kim et al., 2014; Kim et al., 2021).
203   According to the ESR method, land-surface reflectance in the VIS region is constructed
204 from the Top of Atmosphere (TOA) reflectance at 1.6 μm wavelength, based on the NDVI
205 for SWIR and the fraction of urbanization and cropland (Levy et al 2013; Gupta et al., 2016;
206 Zhong et al., 2016; Lim et al., 2018). Ocean-surface reflectance is estimated from the Cox
207 and Munk BRDF model (Cox and Munk, 1954). Chlorophyll-a concentrations are considered
208 in addition to Chlorophyll-a concentration data
209 (https://www.eorc.jaxa.jp/ptree/userguide.html) from Japan Aerospace Exploration Agency
210 (JAXA) (Murakami et al., 2016) and interpolated for the 10-min AHI intervals. For
211 unretrieved pixels, the less contaminated chlorophyll-a concentration value of 0.02 mg m^{-3} is
212 used. Details of the methodology can be found in Lim et al. (2018).

213 **2.2 GOCI aerosol algorithm**

214   GOCI is an ocean color imager in GEO launched onboard COMS in 2010 and observes the
215 East Asia region at an hourly interval with 500 m× 500 m resolution (Choi et al., 2012). It has
216 eight bands in the VIS and NIR regions, which is advantageous for aerosol retrieval. Two
217 versions of GOCI Yonsei aerosol algorithms have been developed, referred to as V1 and V2
218 (Lee et al., 2010; Choi et al., 2016, 2018). In the case of V1, surface reflectance is estimated
219 by the MRM using LER for the past 30 days over land, and the Cox and Munk BRDF model
220 over oceans. In V2, ocean-surface reflectance is estimated by the same method, but land-
221 surface reflectance is improved by using an accumulated long-term database. To minimize
222 the impact of BAOD (the weakness of the MRM), a monthly surface-reflectance database
223 was constructed using all of the LERs over the past five years, but it cannot reflect
224 unexpected changes in surface conditions. However, a well-established climatological
225 database allows aerosol property retrieval in near-real-time with reasonable accuracy.
226

227 **3. Data fusion methods**

228   Satellite-derived AODs have different error characteristics depending on NDVI, scattering
229 angle, and so on (Choi et al., 2016, 2018; Lim et al., 2018). Over oceans, ESR AODs are
230 more accurate than MRM AODs. However, the accuracy of GOCI AODs was dependent on
231 the NDVI values, which represent surface condition in terms of vegetation. V1 has a negative

232   bias and V2 has a mostly a positive bias (Choi et al., 2018). In this study, we developed
233   optimal AOD products at 550 nm in East Asia by fusing four individual retrievals, i.e. two
234   AHI aerosol products from the MRM and ESR methods, and two GOCI products from V1
235   and V2.

3.1 Spatio-temporal matching

237   The AHI and GOCI have different spatial pixel locations and temporal resolutions, so it is
238   necessary to match their spatio-temporal resolutions before data fusion. GOCI and AHI
239   AODs have the same spatial resolution of 6 km × 6 km, but the two satellites are located at
240   128.2° E and 140.7° E, respectively, at the equator. Spatial pixel matching is therefore
241   required. However, satellite-derived AOD represents total-column extinction, so AOD
242   retrieved by the two sensors is not significantly affected by satellite position. To merge the
243   different satellite spatial pixel coverages, the GOCI pixel was re-gridded to match AHI pixels
244   for full-disk observation, with up to 4 GOCI AOD pixels being used with average values
245   considered representative of pixel values. If more than half of the AHI AOD pixels did not
246   exist out of the maximum 6 AHI data per hour, it is regarded as cloud contaminated pixels
247   and an additional cloud removal process is performed. This process applies to both the MRM
248   and ESR method, to remove the AHI's additional cloud-contaminated pixels in products of
249   both GOCI V1 and V2, which have a disadvantage in cloud masking due to their lack of IR
250   channels. When three or more pixels were available for generating AHI data at 1 hour
251   intervals, hourly AOD values were estimated as the medians of pixel values.

3.2 Ensemble-mean method

253   Here, AMR represents AHI MRM AOD, AES represents AHI ESR AOD, GV1 represents
254   GOCI V1 AOD, and GV2 represents GOCI V2 AOD. We performed data fusion using AMR,
255   AES, GV1, and GV2 data within 1 hour intervals for which additional-cloud masking was
256   performed. The ensemble-mean is the mean of the ensemble member over a specific time.
257   The ensemble members are AMR, AES, GV1, and GV2 based on two satellite instruments
258   and two different surface-estimation methodologies. Table 1 provides the satellite-derived
259   AOD used for ensemble-mean and MLE fusion.
260   Fusion was performed only when a pixel of an ensemble member was used for all fusions.
261   Fusion 1 (F1) included the two AHI products of AMR and AES, and two GOCI products of
262   GV1 and GV2. Fusion 2 (F2) involved the calculation of the YAER algorithm by the fusion
263   of AES and GV2, both of which have the advantage of producing data in near-real-time.
264   Fusion 3 (F3) merged AMR and AES to estimate AOD over a wide area, and Fusion 4 (F4)
265   involved a comparison with F1 to determine how accuracy varied with decreasing number of
266   ensemble members, as summarized in Table 1.

3.3 MLE method

268   Similarly, FM1, FM2, and FM3 is the result of MLE fusion corresponding to F1, F2, and F3
269   as in ensemble mean, respectively (see Table 1).
270   The MLE method provides a means of weighting and averaging based on errors evaluated
271   with AERONET ground-based measurements (Nirala, 2008; Xu et al., 2015; Xie et al., 2018).
272   This method employs the following equations:

$$\tau_i^{MLE} = \sum_{k=1}^{N} \frac{R_{i,k}^{-2}}{\sum_{k=1}^{N} R_{i,k}^{-2}} \tau_{i,k} \tag{1}$$

6

$$R_{i,k} = \sqrt{\frac{\sum_{i=1}^{M}(s_{i,k} - g_i)^2}{M}} \qquad (2)$$

273 where τ_i^{MLE} represents the fused AOD; $\tau_{i,k}$ represents the mean AOD at grid point i from the
274 satellite-derived AOD product k, where k is the index for different satellite-derived AOD
275 products for fusion; $R_{i,k}$ represents the root-mean-square error (RMSE) at grid point i for the
276 satellite-derived AOD product k; N is the number of all AOD data; g_i represents the mean of
277 ground-based AOD at grid point i from the AERONET (collocated temporal mean); $s_{i,k}$
278 represents the mean of satellite derived AOD products (k) at grid points of the AERONET
279 (collocated spatial mean); and M is the number of pairs of $s_{i,k}$ and g_i.
280   For RMSE estimation, bias correction, validation, and error estimation (details in Sec.5),
281 AERONET Version 3 Level 2.0 aerosol products were used for ground truth (Giles et al.,
282 2019; Smirnov et al., 2000; Holben et al., 2001). RMSE and bias correction value for each
283 satellite product (details in Sec.3.4) required for MLE fusion were calculated through
284 comparison with AERONET from Apr. 2018 to Mar. 2019 excluding EMeRGe period. The
285 number of AERONET sites used for validation and error estimation in this study, was 35
286 during the KORUS-AQ campaign, and 22 during the EMeRGe campaign, for AHI and GOCI
287 products.
288   Satellite observation can cover wide areas, but the ground observation instrument cannot
289 cover all satellite observed areas. Therefore, a RMSE model was constructed for AOD, time,
290 and NDVI through comparative validation with AERONET observation as shown in Figure 1.
291 For MLE over wide areas without ground measurements, the calculated RMSE from AOD,
292 time, and NDVI bins was applied for every satellite pixel. We excluded points that AOD
293 differences with respect to AERONET data (dAOD) were > 2 standard deviations (SD) to
294 remove outliers and to consider only the more stable RMSE values. According to Figure 1, if
295 the AOD is less than 0.5, RMSE is about 0.1 with respect to all NDVI bins, but if the AOD is
296 greater than 0.5, the overall RMSE value becomes large. All products excluding AES show
297 large variations for high NDVI and high AOD bin as shown as the red square in Figure 1,
298 especially for 02 UTC and 05 UTC of two GOCI products and 00 UTC in AMR product.
299 This is because the two GOCI products and AMR are relatively less accurate for densely
300 vegetated areas, along with sampling issues.

301 **3.4 Bias correction**

302   AOD follows a log-normal distribution (Sayer and Knobelspiesse, 2019), but dAOD for
303 each satellite product follow a Gaussian distribution. The quantile–quantile (Q-Q) plot is a
304 graphical statistical technique that compares two probability distributions with each other.
305 The x-axis represents the quantile value of the directly calculated sample, and the y-axis
306 represents the Z-score. Here, the Z-score is a dimensionless value that makes a statistically
307 Gaussian distribution and shows where each sample is located on the standard deviation. That
308 is, when Z-score of 1 and 2 represent 1 SD and 2 SD, respectively. In addition, ~~as~~ if the Q-Q
309 plot shows a linear shape, the sample is regarded as to follow~~s~~ a Gaussian distribution.
310   Figure 2 shows dAOD divided by SD analyzed for each satellite product, for the period
311 from April 2018 to March 2019, excluding the EMeRGe campaign, which shows a similar
312 pattern to the standard Gaussian distribution. However, if the theoretical quantile values are
313 greater than 0.5, then the sample quantile values are smaller than the standard Gaussian
314 values. Also, when the theoretical quantile is less than 0.5, the opposite results are shown.

7

315 Thus, the sample quantiles are more skewed at both sides than the theoretical quantile, but the
316 respective satellite product is assumed to follows the Gaussian distribution.
317   The bias center for each satellite product was calculated differently for time and NDVI bins
318 through Gaussian fitting in Figure 3 of the dAOD divided by SD (except for 2SD and higher),
319 and subtracted from respective product for correction. Data beyond 2 SD of dAOD were
320 excluded to prevent a change in bias trends due to AOD errors caused by cloud shadows and
321 cloud contamination. This process was performed before applying the MLE method, which
322 allows compensation for systematic bias that is difficult to obtain directly in MLE.
323

324 **3.5 Evaluation of aerosol products during two field campaigns**

325   The performance of the respective satellite product and fused products was analyzed in two
326 field campaigns: the KORUS-AQ of 1 May 2016 to 12 Jun 2016 (https://www-
327 air.larc.nasa.gov/missions/korus-aq/), and the EMeRGe of 12 Mar 2018 to 8 Apr 2018
328 (https://www.halo.dlr.de/science/missions/emerge/emerge.html). KORUS-AQ was an
329 international multi-organization mission to observe air quality across the Korean Peninsula
330 and surrounding waters, led by the US National Aeronautics and Space Administration
331 (NASA) and the Korean National Institute of Environmental Research (NIER) (Crawford et
332 al., 2021). EMeRGe aimed to investigate experimentally the patterns of atmospheric transport
333 and transformation of pollution plumes originating from Eurasia, tropical and subtropical
334 Asian megacities, and other major population centers. GEO satellite data played an important
335 role in these campaigns; e.g., data assimilation for chemical transport models and tracking
336 aerosol plumes (Saide et al., 2014, 2010; Pang et al., 2018).
337   In this study, we used satellite-derived GOCI and AHI AODs, with a spatial resolution of 6
338 km × 6 km, and temporal resolutions of 1 hour and 10 minutes, respectively. Spatio-temporal
339 correlation between satellite-derived AOD and AERONET AOD involved data averaged over
340 all satellite pixels within a 25 km radius of the AERONET site, and AERONET AOD
341 averaged over ±30 minutes from the satellite observation time. As validation metrics,
342 Pearson's correlation coefficient, median bias error (MBE), the fraction (%) within the
343 expected error of MODIS DT (EE), and Global Climate Observing System requirement for
344 AOD (GCOS; GCOS, 2011) were applied. The accuracy requirement of GCOS for satellite-
345 derived AOD at 550nm is 10% or 0.03, whichever is larger. The EE provided by the MODIS
346 DT algorithm (EE as $\pm0.05 \pm 0.15 \times$ AOD; (Levy et al., 2010)) was used for consistent
347 comparison with previous studies.
348   Table 2 shows the validation metrics of the respective product during the two field
349 campaigns. The collocation points for validation with AERONET of two AHI and two GOCI
350 products were not significantly different. %EE and %GCOS of AES and AMR showed better
351 accuracy than GV1 and GV2 during the KORUS and the EMeRGe periods. In terms of MBE,
352 GV2 is 0.008 and -0.001, which shows during the KORUS-AQ and the EMeRGe periods
353 close to zero. Additionally, further analyzes of the respective satellite product are carried out
354 along with fused products in Section 5.
355

356 **4. Results**

357   Figure 4 (a) shows the average AOD of FM1 (MLE method with all products) during the
358 KORUS-AQ period, and Figure 4 (b-e) shows the respective difference of the average AOD
359 of AMR, AES, GV1, and GV2 with respect to FM1. FM1 was selected as the representative

360 fused product as FM1 used all four satellite-derived products for fusion with bias correction.
361 The result of the comparison with the respective satellite product (Figure 4 (b-e)) shows
362 different features. AMR shows a negative bias over the ocean but shows similar results to
363 FM1 over land, while AES shows a different tendency in northern and southern China. GV1
364 tends to show opposite pattern to AES, and GV2 shows positive bias over the ocean and
365 results in similar pattern to FM1 over the land. In the west of the Korean peninsula, AES
366 AOD has a positive offset compared to FM1. Although the AES algorithm considers the
367 fraction of urbanization, there is still a tendency to have a positive AOD offsets. The main
368 reason why AES results show different patterns is the different estimation process of the land
369 surface reflectance from that of other products.
370   On the other hand, in GV1, the AOD over the Manchurian region has a positive offset
371 compared to FM1. This is because the aerosol signal is small over bright surface, making it
372 difficult to retrieve aerosol properties. These features tend to be alleviated in GV2, where the
373 surface reflectance and cloud removal process were improved.
374   Figure 5 shows the same result as Figure 4 except for the EMeRGe period. The AMR and
375 AES AODs appeared high in northern China, which is thought to be the snow contaminated
376 pixel. The EMeRGe period was in March-April, when northern China is more covered by
377 snow compared to the KORUS-AQ period in May-June. On the other hand, for GV1 and
378 GV2, the effect of overestimation with snow contaminated pixel is relatively small, as their
379 snow masking is well performed. However, for the KORUS-AQ period, it seems that the
380 GV1's overestimation of AOD in northern China still remains. Since this analysis (Figure 4
381 and 5) is for the fusion between the three MRM results and one ESR result, the average field
382 difference is naturally the largest in AES which uses ESR method.
383   For the characteristics of the average AOD for the two campaign period, high AODs during
384 the KORUS-AQ period were found in eastern China, and Hokkaido as wildfires from Russia
385 were transported to Hokkaido (Lee et al., 2019). Meanwhile, during the EMeRGe period,
386 high AOD is shown over the Yellow sea as aerosols were transported from China to the
387 Korean peninsula through the west coast, contrary to the KORUS-AQ period. Overall, the
388 average AODs for the EMeRGe are less smooth than those of the KORUS-AQ period. This is
389 because the EMeRGe period was shorter than that of the KORUS-AQ, and the retrieval
390 accuracy was lower due to the bright surface.
391

5. Validation, comparison, and error estimation against AERONET

5.1 Validation for fused AOD products with AERONET

395   The spatio-temporal matching method between fused AOD and AERONET was performed
396 as mentioned above in Section 3.5, and the statistics indices used for verification are also the
397 same. Validation indices of fused products with AERONET AOD during the two campaign
398 periods are summarized in Table 3. During the KORUS-AQ, fused AODs have better
399 accuracy of than respective satellite product in terms of %EE and %GCOS. The %EE
400 and %GCOS of AES, which showed the best accuracy among the respective product, are 63.5%
401 and 43.6%, which are poor than the worst accuracy of the fused AOD. All RMSE has been
402 improved except for FM2. The RMSE of FM2 is higher than RMSE of respective satellite
403 product by 0.001. Although all MBEs show different patterns, the deviation of the fused
404 products tends to be smaller. GV2 and F2 show MBE of 0.008, close to zero.

9

405   Next, %EE for the EMeRGe period exceeded 60.0, with AMR having the best accuracy of
406   69.4. Likewise, %GCOS was also the highest with 52.4, which showed better accuracy than
407   the fused product. In terms of MBE, GV2 was the best, with -0.001. The fused products did
408   not have the best statistical values, but they show overall better statistical values.
409   Figure 6 shows the %GCOS for the respective satellite product and fused products at each
410   validation site during each campaign. In Figure 6(a), for the KORUS period, F1 and FM1
411   show the highest % GCOS at 20 sites out of 35. Other than the fused result, AES shows the
412   highest %GCOS at 13 sites, which are mostly dense vegetation-area and coastal sites. On the
413   other hand, during EMeRGe period, the %GCOS of fused products was highest at 7 sites out
414   of 22, while respective satellite product showed at the rest of the sites in similar proportions.
415

416   **5.2 Error estimation**

417   Differences between satellite products and AERONET, dAOD values were analyzed in
418   terms of NDVI and observation times (Figure 7). Figure 7 (a) and (d) shows the respective
419   satellite product, Figure 7 (b) and (e) the ensemble-mean product, and Figure 7 (c) and (f) the
420   MLE fusion results, with each filled circle representing the mean of 500 and 400 collocated
421   data points sorted in terms of NDVI for the KORUS-AQ and the EMeRGe campaigns,
422   respectively. Figure 7 (a) shows different biases for each satellite product, with AMR and
423   GV1 being negative, AES and GV2 being positive. The errors are close to zero for both the
424   ensemble-mean and MLE products except for FM2 as a result of the fusion process.
425   When the NDVI is small, the mean AOD bias~~Gaussian center~~ for GV2 dAOD was close to
426   zero, but when the NDVI is large, the mean AOD bias~~Gaussian center~~ was negative as shown
427   in Figure 3. The bias correction effect of GV2 shows a small effect for small NDVI bins and
428   a large effect for large NDVI bins. In fact, the collocated dAODs of FM2 show close to zero
429   when the NDVI bins are greater than 0.4 (in Figure 7 (a)).
430   During the EMeRGe campaign (right column, Figure 7), the two AHI and two GOCI
431   products show negative biases, and even the ensemble-mean results have negative biases. The
432   ensemble-mean does not include any bias correction, meaning that the error characteristics of
433   each original satellite product are intact. The MLE products display improved biases in terms
434   of NDVI, which are close to zero because the bias was corrected for in the MLE process.
435   During the EMeRGe period, the collocated dAOD values at NDVI around 0.1 have a
436   negative value for all satellite-derived products (especially AHI products), and GV1 has a
437   negative value for bins where NDVI is greater than 0.2. During the EMeRGe period, the
438   collocated dAOD values at NDVI around 0.1 show negative values for all respective product
439   (especially AHI products), and dAOD for GV1 shows negative values for NDVI bins greater
440   than 0.2. The fused products tend to have error close to zero except for F3 and FM3. In terms
441   of F3, the collocated dAOD value around 0.1 of the NDVI bin has negative values for both
442   AMR and AES, so the collocated dAOD of F3 remain negative. The mean AOD bias
443   ~~Gaussian center~~ values for FM3, AMR and AES (in Figure 3) are close to zero for NDVI at
444   around 0.1, so the bias correction effect is small. This can be explained by the fact that the
445   collocated dAOD for NDVI at around 0.2 during the EMeRGe period is closer to zero in
446   FM3 than in F3.
447   The median bias of the AOD products over the observation time was analyzed as shown in
448   Figure 8 where the left column represents the KORUS-AQ and the right column the EMeRGe
449   campaign, with filled circles representing median values, and the error bar being ±1 SD. As
450   in the KORUS-AQ campaign, the AMR shows a generally negative bias, as in the all-time
451   results, and a negative bias also exists in each time zone. In the AES, GV1, and GV2 case,

452 positive and negative biases appear differently according to time zones. The ±1 SD of the
453 respective satellite product is larger at local noon and smaller at 00 and 07 UTC when SZA is
454 large. Fused products as shown in Figures 8 (b) and (c), have a smaller ±1 SD, and the
455 collocated dAOD over the observation time is also close to zero. Meanwhile, FM2 shows the
456 same tendency of overestimation for the same reason as in the previous Figure 7(a).
457   For the EMeRGe period, the collocated dAOD values of the respective product appear
458 closer to zero than KORUS-AQ. Similarly, the collocated dAOD of the fused products also
459 show values close to zero.
460   The error analysis indicates that the results after fusion are more accurate than the results
461 obtained using individual satellite product, and fused products accuracy was slightly better
462 during KORUS-AQ than EMeRGe because more data points were considered. Also, the
463 surface was relatively dark during the KORUS-AQ period, thus reduced errors for aerosol
464 retrieval than during the EMeRGe period.

465 **5.3 Time-series analysis of daily mean and hourly AODs**

466   The Gangneung-Wonju National University site (Gangneung-WNU; 128.87°E, 37.77°N)
467 lies on the eastern side of the Korean Peninsula and it is one of the regions with low aerosol
468 loadings. The AOD frequency distribution generally follows a log-normal distribution, and it
469 is important to evaluate accuracy for low AOD values. Therefore, we evaluated whether the
470 fused products were improved at low AODs. A daily mean time-series and diurnal variation
471 comparison of different satellite AOD products against AERONET (on a logarithmic scale)
472 are shown in Figure 9 for the Gangneung-WNU site without high AOD events, where most
473 point AERONET AODs at 550 nm were < 1 during the KORUS-AQ campaign. Daily mean
474 time-series data from the AERONET, ensemble-mean, and MLE products are shown in
475 Figure 9 (a-c), where black filled circles and black error bar represent AERONET AOD and
476 ±1 SD of one-day average AERONET AOD. Satellite-derived AODs represented in different
477 colors show similar variabilities.
478   Respective satellite product generally shows similar daily-mean AOD distribution to
479 AERONET AOD. AMR, GV1, GV2 using MRM technique show similar patterns, and AES
480 using SWIR for surface reflectance estimation shows different patterns. The daily-mean AOD
481 of AES is more close to AERONET. On the other hand, Figure 9 (b) and (c) representing
482 fused AOD show similar patterns overall, but the daily-mean AODs on 11 May show
483 different patterns. Here, ensemble-mean products (F1-4) are less accurate than an individual
484 AES product, while MLE products (FM1-3) exhibit similar diurnal variation to daily-mean
485 AERONET AOD. To further analyze this, the daily-mean AOD is shown in Figure 9 (d-f)
486 instead of the hourly AOD for 11- 14 May.
487 As in the previous daily-mean AOD results, Figure 9 (d) shows the hourly AES AOD
488 variations are close to hourly AERONET, while AMR, GV1, and GV2 tend to underestimate.
489 Similarly, as shown in Figure 9 (e), hourly AOD variation of the ensemble-mean products
490 shows overall underestimation for 11 May. All ensemble-mean products use AES as an
491 ensemble member, but do not sufficiently compensate for the negative biases held by AMR,
492 GV1, and GV2. Meanwhile, MLE fused products show similar patterns to the hourly AOD
493 variation of AERONET, such as AES outputs. This can be explained in two ways: the effect
494 of considering the weighted function based on pixel-level uncertainty (RMSE in this study)
495 and the bias correction effects. Figure 1 showed similar RMSE values for all observation
496 times when AOD $\leq$ 0.5. Gangneung-WNU site is one of the densely vegetated areas, but if
497 the AOD is less or equal to 0.5, there is little sensitivity of RMSE according to NDVI bins.
498 That is, regardless of the NDVI, each satellite-specific weighting function used for the MLE

499 fusion has a similar value for all satellite-derived products. The difference between the
500 ensemble-mean and the MLE fused products is due to the bias correction considered in the
501 MLE fusion. For example, the FM3 states that AMR has a large negative bias in the
502 afternoon and AES has a negative bias in the morning. With the bias correction of AES and
503 AMR respectively in the morning and afternoon, FM3 is calibrated in a direction to
504 compensate the underestimated AOD. The effect of bias correction and MLE fusion
505 agreement varies depending on the NDVI and AOD loading for each pixel. If bias correction
506 was not performed in the case on 11 May, the MLE fusion output shows very similar values
507 to F3.
508   The MLE products were implemented in a way to improve accuracy for the low AOD
509 region more critically than in the high AOD region by systematic bias correction. In general
510 surface reflectance estimated by the MRM is affected by BAOD, to result in a negative bias
511 in AOD. On the other hand, the AES uses TOA reflectance at 1.6 μm wavelength to estimate
512 surface reflectance and is therefore less affected by BAOD, and shows higher AOD than
513 AMR and the two GOCI AODs. Furthermore, AOD retrieval over vegetated areas is more
514 accurate with the ESR method. This result is consistent with previous studies of aerosol
515 retrieval in the VIS region (Levy et al., 2013; Gupta et al., 2019; Hsu et al., 2019).
516

517 **5.4 Accuracy evaluation for AHI products of the outside of GOCI domain**

518   In this section, the AMR, AES, F3, and FM3 products were evaluated at 34 sites within the
519 0-50°N and 70-150°E except for the GOCI domain as shown in Figures 4 and 5 (112-148°E,
520 24-50°N). The evaluation results are summarized in Table 4 in terms of N, R, RMSE, MBE,
521 and GCOS fraction. The RMSE and mean AOD bias~~Gaussian center~~ values within the GOCI
522 domain were used in the MLE fusion in this section (see Figures 1 and 3). Table 4 shows
523 the %GCOS and RMSE values with poor accuracy than the validation results for the GOCI
524 coverage as listed in Table 4. In addition, BME during the KORUS-AQ and the EMeRGe
525 period was -0.098 and -0.135 for AMR, and 0.130 and -0.055 for AES, respectively, which
526 show very poor accuracy. This can be explained by the cloud contamination issue at sites
527 near the equator, including Thailand. In addition, since AMR cannot collect enough clear
528 pixels for the estimation of LER, which can cause errors. Furthermore, MRM does not work
529 well over desert areas. On the other hand, AES has issues with poor accuracy over bright
530 pixels such as desert and snow contaminated areas. Second, there are many areas where the
531 coastline is complex as in Hong Kong, and the surface elevation is uneven as in Himalayas.
532 However, there is a bias of -0.055 during the EMeRGe period for AES, but the %GCOS was
533 the highest with 34.1, which is considered significant. F3 and FM3 show similar patterns for
534 the KORUS-AQ and the EMeRGe period. The accuracy of F3 is better than that of FM3,
535 because the previously mentioned issue for the bias correction has worked incorrectly, as the
536 RMSE and bias correction values used were from the data in the untrained area.
537

538 **6. Summary and conclusion**

539   Various aerosol algorithms have been developed for two different GEO satellites, AHI and
540 GOCI. Retrieved AOD data have advantages and disadvantages, depending on the concept of
541 the algorithm and surface-reflectance estimations. In this study, four aerosol products (GV1,
542 GV2, AMR, and AES) were used to construct ensemble-mean and MLE products. For the
543 ensemble-mean, this study presented fusion products taking advantage of overlap region,

544 accuracy, and near-real-time processing. For MLE products, bias corrections for different
545 observation times and surface type were performed considering pixel-level errors, and the
546 synergy of fusion between GEO satellites was successfully demonstrated.
547   Validation with the AERONET confirmed that averaging ensemble members improved
548 most of statistical metrics for ensemble products, and consideration of pixel-level uncertainty
549 further improved the accuracy of MLE products. For optimized AOD products in East Asia,
550 NDVI and time-dependent errors have been reduced. The ensemble-mean and MLE fusion
551 results show consistent results with better accuracy.
552   By comparing F1 and F4, we can see the accuracy changes depending on the number of
553 members used in the ensemble-mean. During the KORUS-AQ period, poor accuracy of each
554 member for ensemble averaging made difficult to find true features. The accuracy of F4 was
555 higher than that of F1, which shows the effect of GV1's large bias during the KORUS-AQ
556 period. On the other hand, for the EMeRGe period, the difference between F1 and F4 appears
557 small because the respective ensemble member's accuracy was better. Both near-real-time
558 products, F2 and FM2, show good accuracy, similar to other fused products. Interestingly, the
559 accuracy of F1 was worse than that of F2, but the accuracy of FM1 was better than that of
560 FM2. The reason for this appears that the long-term RMSE (in Figure 1) and mean AOD bias
561 ~~Gaussian center~~ value (in Figure 3) was a better representation for the EMeRGe than for the
562 KORUS-AQ period. To minimize such errors, overall results can be improved by binning the
563 RMSE and mean AOD bias~~Gaussian center~~ value for the bias correction with respect to
564 month and season in addition to NDVI and time. Naturally, if we directly use the RMSE and
565 mean AOD center~~Gaussian center~~ value of each campaign, the accuracy can be improved.
566   In terms of %GCOS range, satellite-derived and fused products was 33-43% and 46-54%,
567 respectively during the KORUS-AQ, indicating that the fused products have a better or
568 similar statistical score along with other validation scores such as RMSE and MBE. However,
569 the %GCOS during the EMeRGe period shows better accuracy for AMR products with 52.4%
570 than for fused products with a maximum of 47.6%. In terms of other validation indices,
571 however, such as RMSE and MBE, the fused product results represent a better validation
572 score than the AMR. For low aerosol loading case where RMSE is small and similar across
573 different products, bias correction effect was also analyzed at the Gangneung-WNU site by
574 comparing F3 and FM3.
575   As a summary, to increase the accuracy of the fused products, it is required to have either
576 high accuracy of the respective satellite product, or the consistent error characteristics with
577 respect to different parameters such as time, NDVI, etc. If either each satellite-derived AOD
578 is accurate or large numbers of ensemble members are available for compensating respective
579 error, the ensemble-mean shall be the better fusion technique. If the error characteristic is not
580 random and can be expressed as a specific function, the fused product's accuracy through the
581 MLE fusion will be increased.
582   The method applied in this study could be used for AOD fusion of GEO data, such as AMI
583 onboard GK-2A, GOCI-2 and GEMS onboard GK-2B. Furthermore, it is possible to retrieve
584 AOPs other than AOD using multi-angle and multi-channel (UV, VIS, and IR) observations
585 with GK-2A and 2B.
586
587
588 **Code and data availability.**
589
590 The aerosol products data from AHI and GOCI are available on request from the
591 corresponding author (jkim2@yonsei.ac.kr).
592

Author contributions.

HL, SG and JK designed the experiment. HL and SG carried out the data processing. MC, SL, and YK provided support on satellite data. HL wrote the manuscript with contributions from co-authors. JK reviewed and edited the article. JK and CK provided support and supervision. All authors analyzed the measurement data and prepared the article with contributions from all co-authors.

Competing interests.

The authors declare that they have no conflict of interest.

References

Bernard, E., Moulin, C., Ramon, D., Jolivet, D., Riedi, J., and Nicolas, J. M.: Description and validation of an AOT product over land at the 0.6 μm channel of the SEVIRI sensor onboard MSG, Atmospheric Measurement Techniques, 4, 2543-2565, 2011.

Bessho, K., Date, K., Hayashi, M., Ikeda, A., Imai, T., Inoue, H., Kumagai, Y., Miyakawa, T., Murata, H., Ohno, T., Okuyama, A., Oyama, R., Sasaki, Y., Shimazu, Y., Shimoji, K., Sumida, Y., Suzuki, M., Taniguchi, H., Tsuchiyama, H., Uesawa, D., Yokota, H., and Yoshida, R.: An Introduction to Himawari-8/9— Japan’s New-Generation Geostationary Meteorological Satellites, Journal of the Meteorological Society of Japan. Ser. II, 94, 151-183, 2016.

Bilal, M., Nichol, J. E., and Wang, L.: New customized methods for improvement of the MODIS C6 Dark Target and Deep Blue merged aerosol product, Remote Sensing of Environment, 197, 115-124, 2017.

Chatterjee, A., Michalak, A. M., Kahn, R. A., Paradise, S. R., Braverman, A. J., and Miller, C. E.: A geostatistical data fusion technique for merging remote sensing and ground-based observations of aerosol optical thickness, Journal of Geophysical Research, 115, 2010.

Cho, Hi K., Jeong, M. J., Kim, J., Kim, Y. J.: Dependence of diffuse photosynthetically active solar irradiance on total optical depth, Journal of Geophysical Research, 108, D9, 4267, 4-1~4-10, 2003.

14

637
638 Choi, J.-K., Park, Y. J., Ahn, J. H., Lim, H.-S., Eom, J., and Ryu, J.-H.: GOCI, the world's first geostationary
639 ocean color observation satellite, for the monitoring of temporal variability in coastal water turbidity, Journal of
640 Geophysical Research: Oceans, 117, C9, 2012.

641 Choi, M., Kim, J., Lee, J., Kim, M., Park, Y.-J., Jeong, U., Kim, W., Hong, H., Holben, B. N., Eck, T. F., Song,
642 C. H., Lim, J.-H., and Song, C.-K.: GOCI Yonsei Aerosol Retrieval (YAER) algorithm and validation during
643 the DRAGON-NE Asia 2012 campaign, Atmos. Meas. Tech., 9, 1377-1398, 2016.

644 Choi, M., Kim, J., Lee, J., Kim, M., Park, Y.-J., Holben, B., Eck, T. F., Li, Z., and Song, C. H.: GOCI Yonsei
645 aerosol retrieval version 2 products: an improved algorithm and error analysis with uncertainty estimation from
646 5-year validation over East Asia, Atmospheric Measurement Techniques, 11, 385-408, 2018.

647 Cox, C.: Statistics of the sea surface derived from sun glitter, J. Marine Research, 13, 198-227, 1954.

648 Crawford, J., J.-Y. Ahn, J. Al-Saadi, L. Chang, L. K. Emmons, J. Kim, G. Lee, J.-H. Park, R. J. Park, J. H. Woo,
649 C.-K. Song, J.-H. Hong, Y.-D. Hong, B. L. Lefer, M. Lee, T.Lee, S. Kim, K.-E. Min, S. S. Yum, H. J. Shin, Y.-
650 W. Kim, J.-S. Choi, J.-S. Park, J. J. Szykman, R. W. Long, C. E. Jordan, I. J. Simpson, A. Fried, J. E. Dibb, S.Y.
651 Cho, and Y. P. Kim: The Korea-United States Air Quality (KORUS-AQ) Field Study, Elementa, revised, 2021
652
653 Fukuda, S., Nakajima, T., Takenaka, H., Higurashi, A., Kikuchi, N., Nakajima, T. Y., and Ishida, H.: New
654 approaches to removing cloud shadows and evaluating the 380 nm surface reflectance for improved aerosol
655 optical thickness retrievals from the GOSAT/TANSO-Cloud and Aerosol Imager, Journal of Geophysical
656 Research: Atmospheres, 118, 13,520-513,531, 2013.

657 Garay, M. J., Kalashnikova, O. V., and Bull, M. A.: Development and assessment of a higher-spatial-resolution
658 (4.4 km) MISR aerosol optical depth product using AERONET-DRAGON data, Atmospheric Chemistry and
659 Physics, 17, 5095-5106, 2017.

660 Garay, M. J., Witek, M. L., Kahn, R. A., Seidel, F. C., Limbacher, J. A., Bull, M. A., Diner, D. J., Hansen, E. G.,
661 Kalashnikova, O. V., Lee, H., Nastan, A. M., and Yu, Y.: Introducing the 4.4&#8201;km spatial resolution
662 Multi-Angle Imaging SpectroRadiometer (MISR) aerosol product, Atmospheric Measurement Techniques, 13,
663 593-628, 2020.

664 GCOS, W.: Systematic Observation Requirements for Satellite–BASED Data Products for Climate, 154
665 Document. 2011.
666
667 Giles, D. M., Sinyuk, A., Sorokin, M. S., Schafer, J. S., Smirnov, A., Slutsker, I., Eck, T. F., Holben, B. N.,
668 Lewis, J., Campbell, J., Welton, E. J., Korkin, S., and Lyapustin, A.: Advancements in the Aerosol Robotic
669 Network (AERONET) Version 3 Database – Automated Near Real-Time Quality Control Algorithm with
670 Improved Cloud Screening for Sun Photometer Aerosol Optical Depth (AOD) Measurements, Atmos. Meas.
671 Tech. Discuss., doi: https://doi.org/10.5194/amt-2018-272, 2018. 2018.

672 Go, S., Kim, J., Park, S. S., Kim, M., Lim, H., Kim, J.-Y., Lee, D.-W., and Im, J.: Synergistic Use of
673 Hyperspectral UV-Visible OMI and Broadband Meteorological Imager MODIS Data for a Merged Aerosol
674 Product, Remote Sensing, 12, 2020.
675
676 Gupta, P., Patadia, F., and Christopher, S. A.: Multisensor Data Product Fusion for Aerosol Research, IEEE
677 Transactions on Geoscience and Remote Sensing, 46, 1407-1415, 2008.

678 Gupta, P., Levy, R. C., Mattoo, S., Remer, L. A., and Munchak, L. A.: A surface reflectance scheme for
679 retrieving aerosol optical depth over urban surfaces in MODIS Dark Target retrieval algorithm, Atmospheric
680 Measurement Techniques, 9, 3293-3308, 2016.

681 Gupta, P., Levy, R. C., Mattoo, S., Remer, L. A., Holz, R. E., and Heidinger, A. K.: Applying the Dark Target
682 aerosol algorithm with Advanced Himawari Imager observations during the KORUS-AQ field campaign, 2019.
683 2019.

684 Herman, J., Bhartia, P., Torres, O., Hsu, C., Seftor, C., and Celarier, E.: Global distribution of UV-absorbing
685 aerosols from Nimbus 7/TOMS data, Journal of Geophysical Research: Atmospheres, 102, 16911-16922, 1997.

686 Holben, B. N., Tanre, D., Smirnov, A., Eck, T., Slutsker, I., Abuhassan, N., Newcomb, W., Schafer, J., Chatenet,
687 B., and Lavenu, F. J. J. o. G. R. A.: An emerging ground-based aerosol climatology: Aerosol optical depth from
688 AERONET, 106, 12067-12097, 2001.

689 Hsu, N. C., Tsay, S.-C., King, M. D., Herman, J. R. I. T. o. G., and Sensing, R.: Aerosol properties over
690 bright-reflecting source regions, 42, 557-569, 2004.

691 Hsu, N., Jeong, M. J., Bettenhausen, C., Sayer, A., Hansell, R., Seftor, C., Huang, J., and Tsay, S. C.: Enhanced
692 Deep Blue aerosol retrieval algorithm: The second generation, Journal of Geophysical Research: Atmospheres,
693 118, 9296-9315, 2013.

694 Hsu, N., Lee, J., Sayer, A., Kim, W., Bettenhausen, C., and Tsay, S. C. J. J. o. G. R. A.: VIIRS Deep Blue
695 aerosol products over land: Extending the EOS long-term aerosol data records, 124, 4026-4053, 2019.

696 Jackson, J. M., Liu, H., Laszlo, I., Kondragunta, S., Remer, L. A., Huang, J., and Huang, H.-C.: Suomi-NPP
697 VIIRS aerosol algorithms and data products, Journal of Geophysical Research: Atmospheres, 118, 12,673-
698 612,689, 2013.

699 Kikuchi, M., Murakami, H., Suzuki, K., Nagao, T. M., and Higurashi, A.: Improved Hourly Estimates of
700 Aerosol Optical Thickness Using Spatiotemporal Variability Derived From Himawari-8 Geostationary Satellite,
701 IEEE Transactions on Geoscience and Remote Sensing, 56, 3442-3455, 2018.

702 Kim, J., Lee, J., Lee, H. C., Higurashi, A., Takemura, T., and Song, C. H., Consistency of the aerosol type
703 classification from satellite remote sensing during the Atmospheric Brown Cloud–East Asia Regional
704 Experiment campaign, J. Geophys. Res., 112, D22S33, doi:10.1029/2006JD008201, 2007.

705 Kim, J., Yoon, J. M., Ahn, M. H., Sohn, B. J., and Lim, H. S.: Retrieving aerosol optical depth using visible and
706 mid-IR channels from geostationary satellite MTSAT-1R, International Journal of Remote Sensing, 29, 6181-
707 6192, 2008.

708 Kim, J., Kim, M., and Choi, M.: Monitoring aerosol properties in east Asia from geostationary orbit: GOCI, MI
709 and GEMS. In: Air Pollution in Eastern Asia: An Integrated Perspective, Springer, 2017.

710 Kim, J., Jeong, U., Ahn, M.-H., Kim, J. H., Park, R. J., Lee, H., Song, C. H., Choi, Y.-S., Lee, K.-H., Yoo, J.-M.,
711 Jeong, M.-J., Park, S. K., Lee, K.-M., Song, C.-K., Kim, S.-W., Kim, Y. J., Kim, S.-W., Kim, M., Go, S., Liu,
712 X., Chance, K., Chan Miller, C., Al-Saadi, J., Veihelmann, B., Bhartia, P. K., Torres, O., Abad, G. G., Haffner,
713 D. P., Ko, D. H., Lee, S. H., Woo, J.-H., Chong, H., Park, S. S., Nicks, D., Choi, W. J., Moon, K.-J., Cho, A.,
714 Yoon, J., Kim, S.-k., Hong, H., Lee, K., Lee, H., Lee, S., Choi, M., Veefkind, P., Levelt, P. F., Edwards, D. P.,
715 Kang, M., Eo, M., Bak, J., Baek, K., Kwon, H.-A., Yang, J., Park, J., Han, K. M., Kim, B.-R., Shin, H.-W., Choi,
716 H., Lee, E., Chong, J., Cha, Y., Koo, J.-H., Irie, H., Hayashida, S., Kasai, Y., Kanaya, Y., Liu, C., Lin, J.,
717 Crawford, J. H., Carmichael, G. R., Newchurch, M. J., Lefer, B. L., Herman, J. R., Swap, R. J., Lau, A. K. H.,
718 Kurosu, T. P., Jaross, G., Ahlers, B., Dobber, M., McElroy, C. T., and Choi, Y.: New Era of Air Quality
719 Monitoring from Space: Geostationary Environment Monitoring Spectrometer (GEMS), Bulletin of the
720 American Meteorological Society, 101, E1-E22, 2020.

721 Kim, M., Kim, J., Wong, M. S., Yoon, J., Lee, J., Wu, D., Chan, P. W., Nichol, J. E., Chung, C.-Y., and Ou, M.-
722 L.: Improvement of aerosol optical depth retrieval over Hong Kong from a geostationary meteorological satellite
723 using critical reflectance with background optical depth correction, Remote Sensing of Environment, 142, 176-
724 187, 2014.

725 Kim, M., Kim, J., Jeong, U., Kim, W., Hong, H., Holben, B., Eck, T. F., Lim, J. H., Song, C. K., Lee, S., and
726 Chung, C. Y.: Aerosol optical properties derived from the DRAGON-NE Asia campaign, and implications for a
727 single-channel algorithm to retrieve aerosol optical depth in spring from Meteorological Imager (MI) on-board
728 the Communication, Ocean, and Meteorological Satellite (COMS), Atmos. Chem. Phys., 16, 1789-1808, 2016.

729 Kim, M., Kim, S. H., Kim, W. V., Lee, Y. G., Kim, J., and Kafatos, M. C.: Assessment of Aerosol optical depth
730 under background and polluted conditions using AERONET and VIIRS datasets, Atmospheric Environment,
731 245, 2021.
732 Knapp, K. R., Frouin, R., Kondragunta, S., and Prados, A.: Toward aerosol optical depth retrievals over land
733 from GOES visible radiances: determining surface reflectance, International Journal of Remote Sensing, 26,
734 4097-4116, 2007.

Koelemeijer, R., De Haan, J., and Stammes, P.: A database of spectral surface reflectivity in the range 335–772 nm derived from 5.5 years of GOME observations, Journal of Geophysical Research: Atmospheres, 108, 2003.

Lee, J., Kim, J., Song, C. H., Ryu, J.-H., Ahn, Y.-H., and Song, C.: Algorithm for retrieval of aerosol optical properties over the ocean from the Geostationary Ocean Color Imager, Remote Sensing of Environment, 114, 1077-1088, 2010.

Lee, J., Kim, J., Yang, P., and Hsu, N. C.: Improvement of aerosol optical depth retrieval from MODIS spectral reflectance over the global ocean using new aerosol models archived from AERONET inversion data and tri-axial ellipsoidal dust database, Atmospheric Chemistry and Physics, 12, 7087-7102, 2012.

Levy, R. C., Remer, L. A., Kleidman, R. G., Mattoo, S., Ichoku, C., Kahn, R., and Eck, T. F.: Global evaluation of the Collection 5 MODIS dark-target aerosol products over land, Atmospheric Chemistry and Physics, 10, 10399-10420, 2010.

Levy, R. C., Mattoo, S., Munchak, L. A., Remer, L. A., Sayer, A. M., Patadia, F., and Hsu, N. C.: The Collection 6 MODIS aerosol products over land and ocean, Atmospheric Measurement Techniques, 6, 2989-3034, 2013.

Lee, S., Kim, M., Choi, M., Go, S., Kim, J., Kim, J.-H., Lim, H.-K., Jeong, U., Goo, T.-Y., Kuze, A., Shiomi, K., and Tatsuya, Y.: Aerosol Property Retrieval Algorithm over Northeast Asia from TANSO-CAI Measurements Onboard GOSAT, Remote Sensing, 9, 2017.

Lee, S., Kim, J., Choi, M., Hong, J., Lim, H., Eck, T. F., Holben, B. N., Ahn, J.-Y., Kim, J., and Koo, J.-H.: Analysis of long-range transboundary transport (LRTT) effect on Korean aerosol pollution during the KORUS-AQ campaign, Atmospheric Environment, 204, 53-67, 2019.

Li, L., Shi, R., Zhang, L., Zhang, J., and Gao, W.: The data fusion of aerosol optical thickness using universal kriging and stepwise regression in East China, 2014, 922112.

Lim, H., Choi, M., Kim, M., Kim, J., and Chan, P. W.: Retrieval and Validation of Aerosol Optical Properties Using Japanese Next Generation Meteorological Satellite, Himawari-8, Korean Journal of Remote Sensing, 32, 681-691, 2016.

Lim, H., Choi, M., Kim, J., Kasai, Y., and Chan, P.: AHI/Himawari-8 Yonsei Aerosol Retrieval (YAER): Algorithm, Validation and Merged Products, Remote Sens., 10, 2018.

Lyapustin, A., Martonchik, J., Wang, Y., Laszlo, I., and Korkin, S.: Multiangle implementation of atmospheric correction (MAIAC): 1. Radiative transfer basis and look-up tables, Journal of Geophysical Research, 116, 2011a.

Lyapustin, A., Wang, Y., Laszlo, I., Kahn, R., Korkin, S., Remer, L., Levy, R., and Reid, J. S.: Multiangle implementation of atmospheric correction (MAIAC): 2. Aerosol algorithm, Journal of Geophysical Research, 116, 2011b.

Lyapustin, A., Wang, Y., Korkin, S., and Huang, D.: MODIS Collection 6 MAIAC algorithm, Atmospheric Measurement Techniques, 11, 5741-5765, 2018.

Mélin, F., Zibordi, G., and Djavidnia, S.: Development and validation of a technique for merging satellite derived aerosol optical depth from SeaWiFS and MODIS, Remote Sensing of Environment, 108, 436-450, 2007.

Murakami, H.: Ocean color estimation by Himawari-8/AHI, 2016, 987810.

Negi, H. and Kokhanovsky, A. J. T. C.: Retrieval of snow albedo and grain size using reflectance measurements in Himalayan basin, 5, 203, 2011.

Nguyen, H., Cressie, N., and Braverman, A.: Spatial Statistical Data Fusion for Remote Sensing Applications, Journal of the American Statistical Association, 107, 1004-1018, 2012.

Nirala, M.: Technical Note: Multi-sensor data fusion of aerosol optical thickness, International Journal of Remote Sensing, 29, 2127-2136, 2008.

781 Pang, J., Liu, Z., Wang, X., Bresch, J., Ban, J., Chen, D., and Kim, J.: Assimilating AOD retrievals from GOCI
782 and VIIRS to forecast surface PM2.5 episodes over Eastern China, Atmospheric Environment, 179, 288-304,
783 2018.

784 Remer, L. A., Kaufman, Y., Tanré, D., Mattoo, S., Chu, D., Martins, J. V., Li, R.-R., Ichoku, C., Levy, R., and
785 Kleidman, R.: The MODIS aerosol algorithm, products, and validation, Journal of the atmospheric sciences, 62,
786 947-973, 2005.

787 Remer, L. A., Mattoo, S., Levy, R. C., and Munchak, L.: MODIS 3 km aerosol product: algorithm and global
788 perspective, Atmospheric Measurement Techniques Discussions, 6, 69-112, 2013.

789 Saide, P. E., Kim, J., Song, C. H., Choi, M., Cheng, Y., and Carmichael, G. R.: Assimilation of next generation
790 geostationary aerosol optical depth retrievals to improve air quality simulations, Geophysical Research Letters,
791 41, 9188-9196, 2014.

792 Saide, P. E., Gao, M., Lu, Z., Goldberg, D., Streets, D. G., Woo, J.-H., Beyersdorf, A., Corr, C. A., Thornhill, K.
793 L., Anderson, B., Hair, J. W., Nehrir, A. R., Diskin, G. S., Jimenez, J. L., Nault, B. A., Campuzano-Jost, P.,
794 Dibb, J., Heim, E., Lamb, K. D., Schwarz, J. P., Perring, A. E., Kim, J., Choi, M., Holben, B., Pfister, G.,
795 Hodzic, A., Carmichael, G. R., Emmons, L., and Crawford, J. H. : Understanding and improving model
796 representation of aerosol optical properties for a Chinese haze event measured during KORUS-AQ,
797 Atmospheric Chemistry and Physics, 20, 6455-6478,2020.
798
799 Sayer, A., Munchak, L., Hsu, N., Levy, R., Bettenhausen, C., and Jeong, M. J.: MODIS Collection 6 aerosol
800 products: Comparison between Aqua's e-Deep Blue, Dark Target, and "merged" data sets, and usage
801 recommendations, Journal of Geophysical Research: Atmospheres, 119, 2014.

802 Sayer, A., Hsu, N., Lee, J., Bettenhausen, C., Kim, W., and Smirnov, A. J. J. o. G. R. A.: Satellite Ocean
803 Aerosol Retrieval (SOAR) Algorithm Extension to S-NPP VIIRS as Part of the "Deep Blue" Aerosol Project,
804 123, 380-400, 2018.

805 Sayer, A. M., Hsu, N. C., Lee, J., Kim, W. V., and Dutcher, S. T.: Validation, Stability, and Consistency of
806 MODIS Collection 6.1 and VIIRS Version 1 Deep Blue Aerosol Data Over Land, Journal of Geophysical
807 Research: Atmospheres, 124, 4658-4688, 2019.

808 Smirnov, A., Holben, B. N., Eck, T. F., Dubovik, O., and Slutsker, I.: Cloud screening and quality control
809 algorithms for the AERONET data base, Remote Sens. Environ., 73, 337-349, 2000.

810 Stocker, T. F., Qin, D., Plattner, G.-K., Tignor, M., Allen, S. K., Boschung, J., Nauels, A., Xia, Y., Bex, B., and
811 Midgley, B.: IPCC, 2013: climate change 2013: the physical science basis. Contribution of working group I to
812 the fifth assessment report of the intergovernmental panel on climate change. Cambridge University Press, 2013.

813 Tang, Q., Bo, Y., and Zhu, Y.: Spatiotemporal fusion of multiple-satellite aerosol optical depth (AOD) products
814 using Bayesian maximum entropy method, Journal of Geophysical Research: Atmospheres, 121, 4034-4048,
815 2016.

816 Wang, J.: Geostationary satellite retrievals of aerosol optical thickness during ACE-Asia, Journal of
817 Geophysical Research, 108, 2003.

818 Wang, J., Brown, D. G., and Hammerling, D.: Geostatistical inverse modeling for super-resolution mapping of
819 continuous spatial processes, Remote Sensing of Environment, 139, 205-215, 2013.

820 Wei, J., Li, Z., Sun, L., Peng, Y., and Wang, L.: Improved merge schemes for MODIS Collection 6.1 Dark
821 Target and Deep Blue combined aerosol products, Atmospheric Environment, 202, 315-327, 2019.Xie, Y., Xue,
822 Y., Che, Y., Guang, J., Mei, L., Voorhis, D., Fan, C., She, L., Xu, H. J. I. T. o. G., and Sensing, R.: Ensemble of
823 ESA/AATSR aerosol optical depth products based on the likelihood estimate method with uncertainties, 56,
824 997-1007, 2018.

825 Xu, H., Guang, J., Xue, Y., De Leeuw, G., Che, Y., Guo, J., He, X., and Wang, T. J. A. E.: A consistent aerosol
826 optical depth (AOD) dataset over mainland China by integration of several AOD products, 114, 48-56, 2015.

827   Xue, Y., Xu, H., Mei, L., Guang, J., Guo, J., Li, Y., Hou, T., Li, C., Yang, L., He, X. J. A. C., and Discussions,
828   P.: Merging aerosol optical depth data from multiple satellite missions to view agricultural biomass burning in
829   Central and East China, 12, 10461-10492, 2012.

830

831   Yoon, J. M., Kim, J., Lee, J. H., Cho, H. K., Sohn, B.-J., and Ahn, M.-H. J. A.-P. J. o. A. S.: Retrieval of aerosol
832   optical depth over East Asia from a geostationary satellite, MTSAT-1R, 43, 49-58, 2007.

833   Yoshida, M., Kikuchi, M., Nagao, T. M., Murakami, H., Nomaki, T., and Higurashi, A.: Common Retrieval of
834   Aerosol Properties for Imaging Satellite Sensors, Journal of the Meteorological Society of Japan. Ser. II, 96B,
835   193-209, 2018.

836   Zhong, G., Wang, X., Tani, H., Guo, M., Chittenden, A., Yin, S., Sun, Z., and Matsumura, S.: A Modified
837   Aerosol Free Vegetation Index Algorithm for Aerosol Optical Depth Retrieval Using GOSAT TANSO-CAI
838   Data, Remote Sensing, 8, 2016.

839

840 Table 1. Satellite dataset used for the fusion products. Four entries F1-F4, and three entries FM1-FM3 represent
841 ensemble-mean fusion and MLE fusion products.

AOD type	F1	F2	F3	F4	FM1	FM2	FM3
AER	o	o	o	o	o	o	o
AMR	o		o	o	o		o
GV1	o				o		
GV2	o	o		o	o	o	
Remark					MLE Products[2]		
	All available products	For NRT[1]	AHI only for wider area	Without GV1 to check missing effect	Same as F1	Same as F2	Same as F3

842 [1] NRT: near real time; [2] Maximum Likelihood Estimation
843

844
845
846
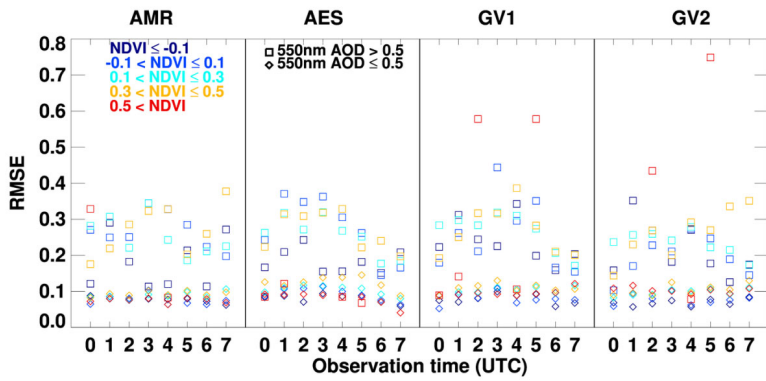
847
848 Figure 1. RMSE according to NDVI (color), observation time, and satellite AODs (square and diamond
849 represent AOD at 550nm greater and less equal than 0.5) during Apr. 2018 to Mar. 2019 excluding EMeRGe
850 campaign. Colors represent different NDVI bins.

851

852
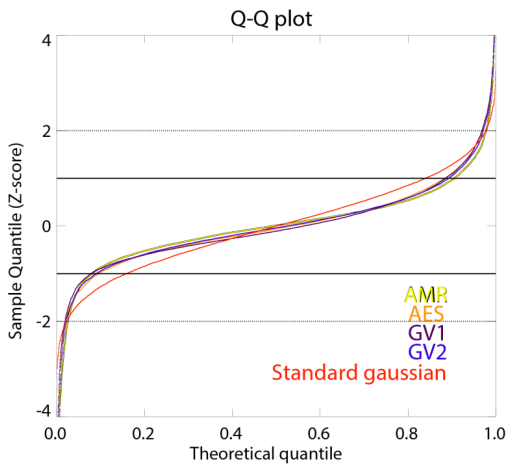
853
854 Figure 2. Q-Q plot for the difference between AERONET AOD and AMR(~~purple~~yellow), AES(~~orange~~cyan),
855 GV1(~~green~~purple), and GV2(~~orange~~dark blue) AOD. The black solid line and dotted line represent 1-σ and 2-σ,
856 respectively.

857
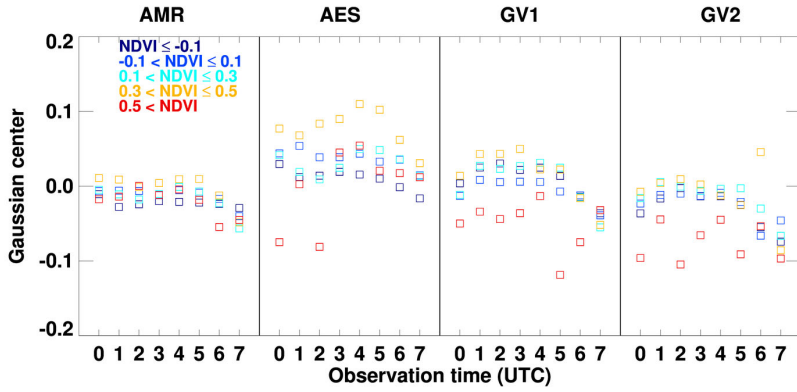
858
859 Figure 3. Systematic bias-correction values for NDVI groups and temporal bins for each satellite product from
860 Gaussian fitting analysis used in MLE fusion.

861
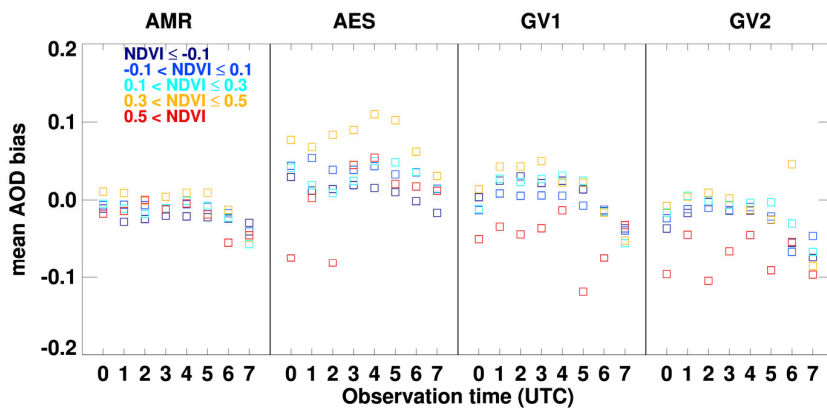
862 Figure 33. Systematic bias-correction values for NDVI groups and temporal bins for each satellite product from
863 Gaussian fitting analysis used in MLE fusion. Colors represent different NDVI bins.

864

865 Table 2. Validation statistics of the respective satellite product during the KORUS-AQ and the EMeRGe
866 campaign.

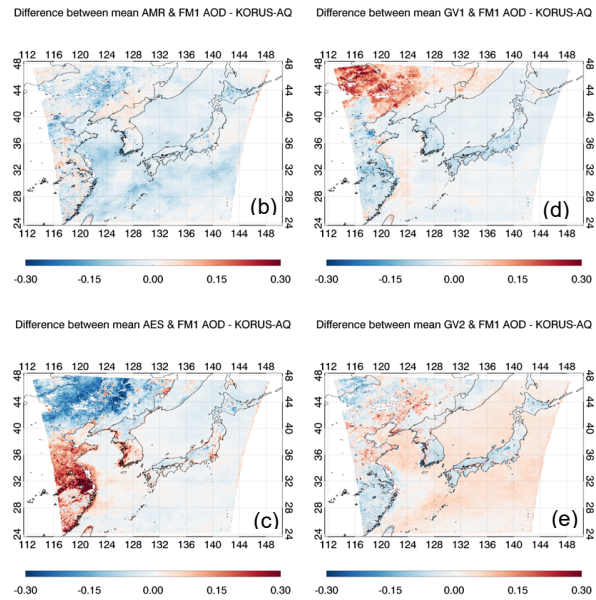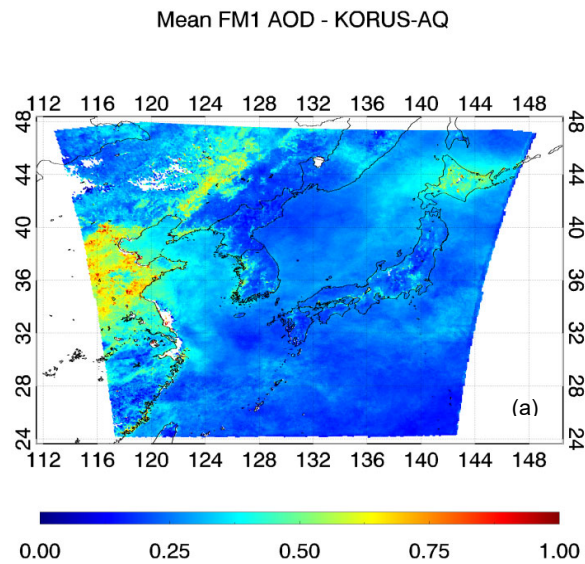| Product type	KORUS-AQ					EMeRGe				
	%EE	%GCOS	RMSE	MBE	N	%EE	%GCOS	RMSE	MBE	N
AES	63.5	43.6	0.145	0.029	5069	65.2	46.3	0.176	-0.011	1884
AMR	60.6	39.4	0.150	-0.054	5069	69.4	52.4	0.162	-0.028	1884
GV1	52.2	34.7	0.153	-0.045	4843	63.4	42.7	0.162	-0.035	1760
GV2	50.3	33.8	0.176	0.008	4924	61.5	41.8	0.164	-0.001	1863

867
868

Figure 4. The average AOD of (a) FM1 (AMR, AES, GV1, and GV2) during the KORUS AQ. The difference of mean (b)AMR, (c)AES, (d) GV1, and (e) GV2 AODs with respect to mean representative (FM1) AOD. Figures generated with Interactive Data Language (IDL) version 8.8.0.
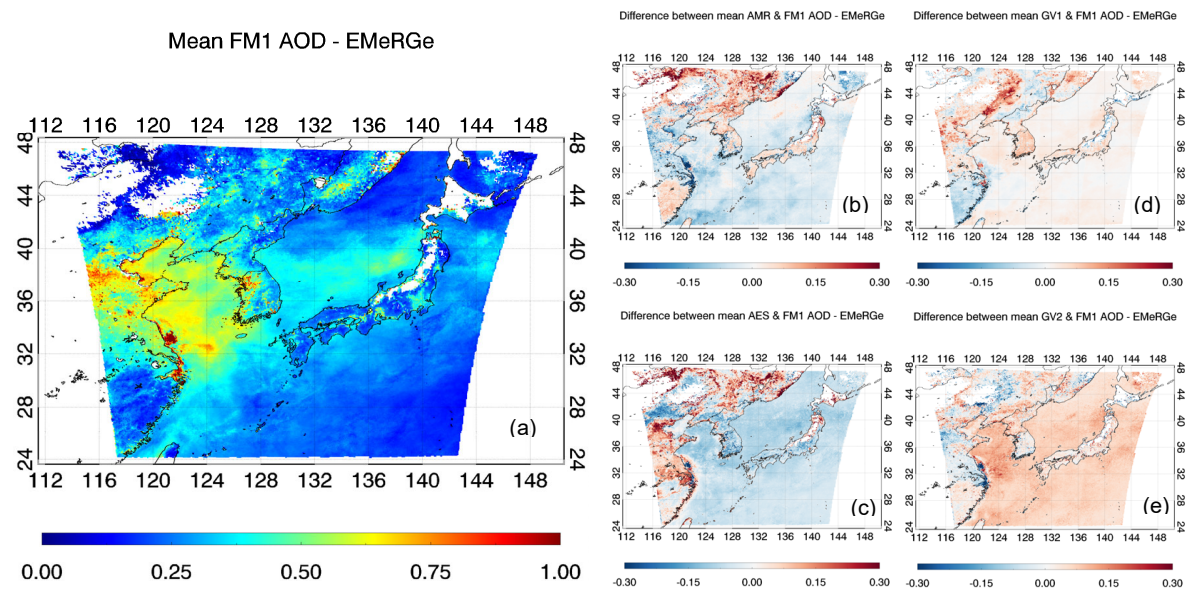
Mean FM1 AOD - EMeRGe

Difference between mean AMR & FM1 AOD - EMeRGe

Difference between mean GV1 & FM1 AOD - EMeRGe

Difference between mean AES & FM1 AOD - EMeRGe

Difference between mean GV2 & FM1 AOD - EMeRGe

Figure 5. Same as Figure 4, but for EMeRGe campaign.

25

Table 3. Validation statistics of the ensemble-mean fusion (F1-F4), and MLE fusion (FM1-FM4) AOD during two field campaigns (left: KORUS-AQ, right: EMeRGe).

| Fusion method	Product type	KORUS-AQ					EMeRGe				
		%EE	%GCOS	RMSE	MBE	N	%EE	%GCOS	RMSE	MBE	N
Ensemble-mean	F1	67.8	47.2	0.134	-0.014	4806	66.8	45.4	0.149	-0.012	1754
	F2	72.3	52.7	0.129	0.008	4843	66.9	45.5	0.150	-0.012	1760
	F3	72.1	51.1	0.133	0.012	5069	63.2	44.5	0.175	-0.019	1884
	F4	73.3	51.6	0.128	-0.015	4843	66.4	44.8	0.153	-0.024	1760
MLE	FM1	72.6	52.4	0.130	-0.012	4806	69.1	47.6	0.147	-0.008	1754
	FM2	65.5	46.1	0.146	0.034	4924	67.3	46.5	0.152	0.014	1863
	FM3	75.2	54.5	0.129	-0.09	5069	62.4	41.8	0.177	-0.027	1884

5
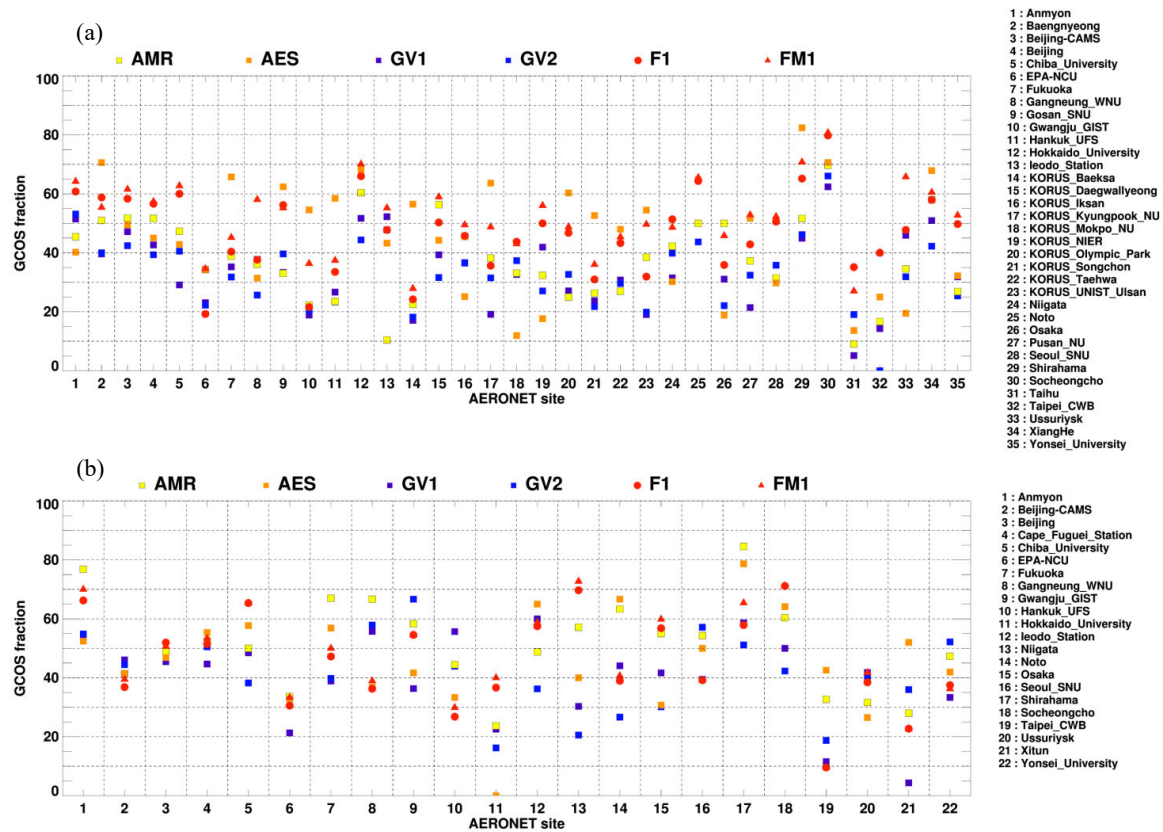
Figure 6. Comparison of the GCOS fraction for respective satellite (AMR, AES, GV1, and GV2), ensemble-mean fusion (F1), and MLE fusion (FM1) during the (a) KORUS-AQ and (b) EMeRGe campaign. Colors represent different aerosol products.
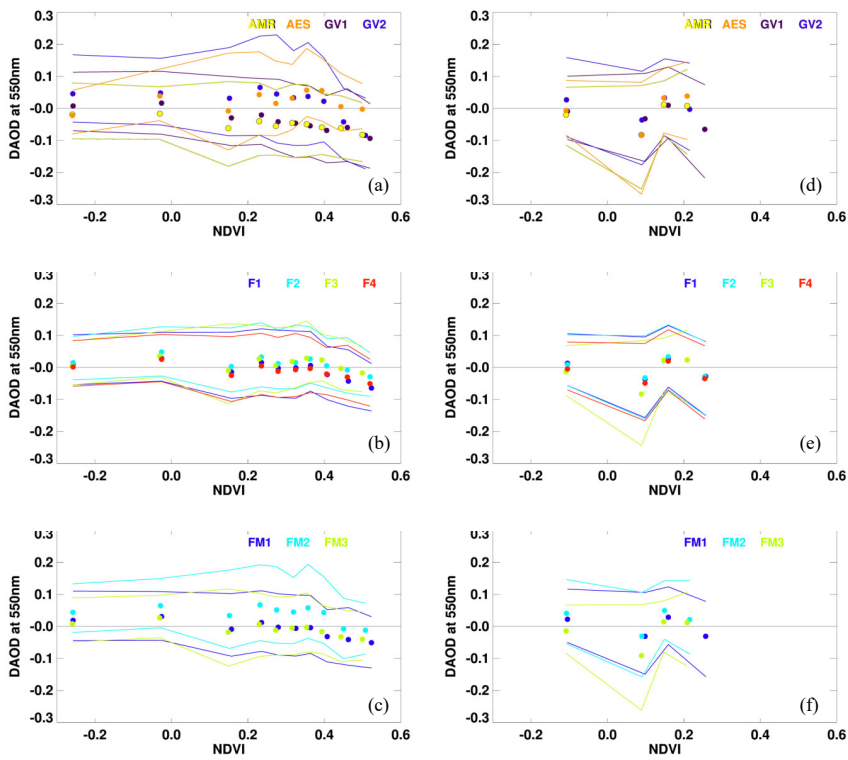
Figure 7. Difference between (a, d) respective, (b, e) ensemble-mean, or (c, f) MLE and AERONET AOD in terms of NDVI during the KORUS-AQ (left column) and the EMeRGe (right column) campaigns. Each points and solid lines represent the median and 1-σ (16th and 84th percentile) of 500 (for the KORUS-AQ) and 400 (for the EMeRGe) collocated data points in terms of NDVI values, respectively. Colors represent different aerosol products.
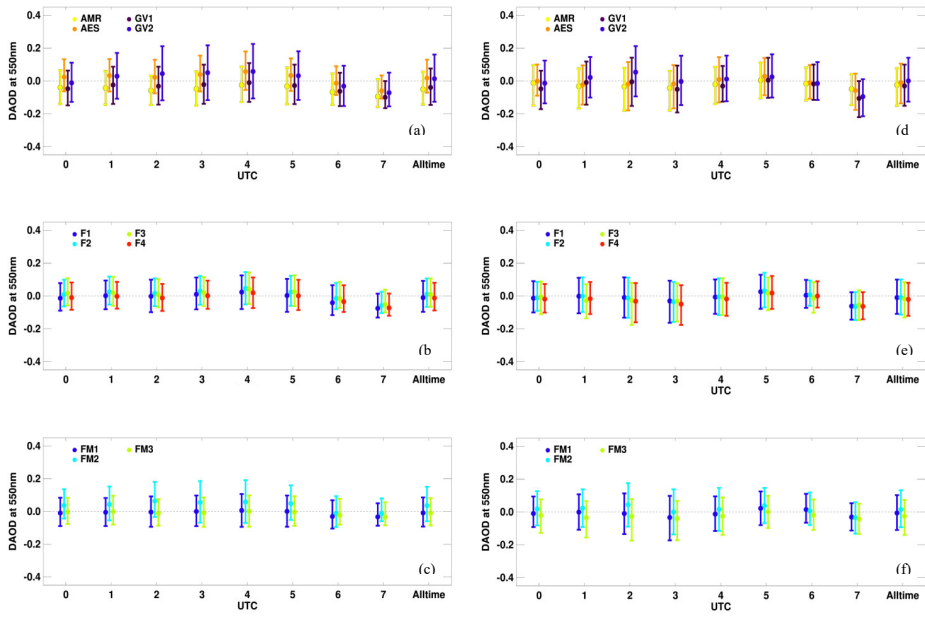
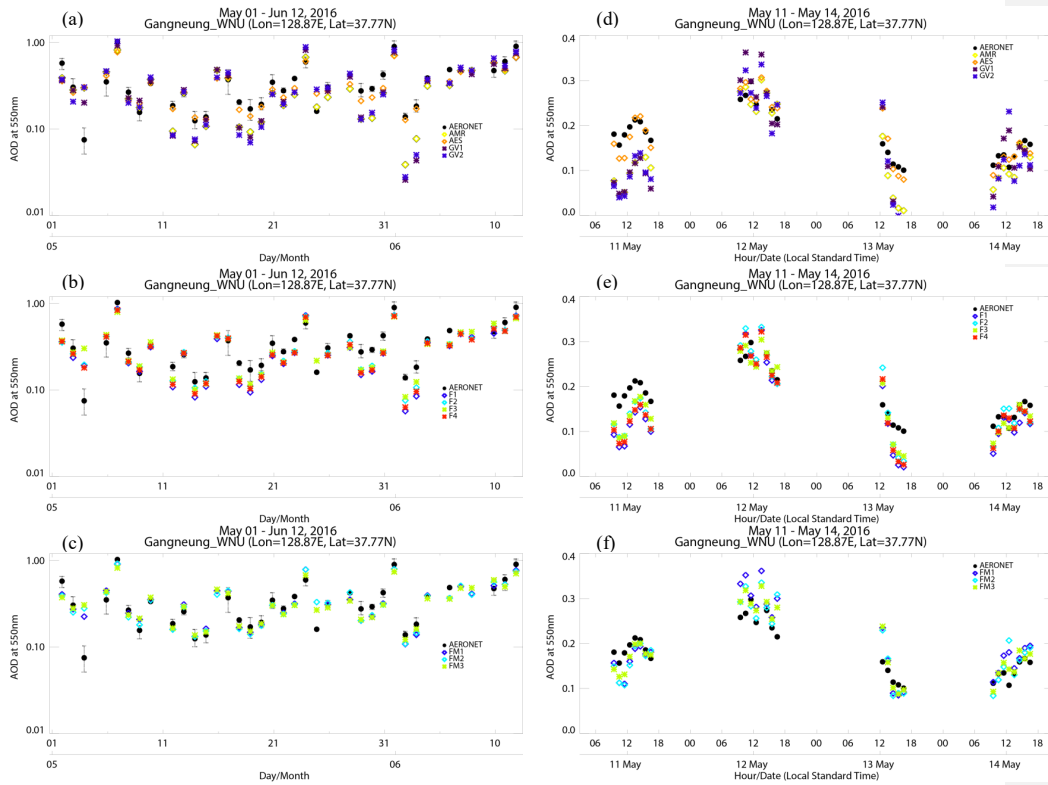Figure 8. Same as Figure78, but for the observation time in UTC.

Figure 9. Time series of the daily average AODs at Gangneung WNU site during the KORUS-AQ campaign from (a) respective satellite, (b) ensemble-mean, and (c) MLE fusion. The black-filled circle represents AERONET AOD, and the error bar represents 1-SD of daily AERONET AODs. The diurnal variation in AODs from 11 to 14 May 2016 is shown in the right column, where (d) is the respective satellite, (e) is fused, and (f) is MLE products.

Table 4. Accuracy evaluation of outside of GOCI area of AMR, AES, F3, and FM3 AODs.

Without GOCI domain	KORUS-AQ AMR	KORUS-AQ AES	KORUS-AQ F3	KORUS-AQ FM3	EMeRGe AMR	EMeRGe AES	EMeRGe F3	EMeRGe FM3
N	1959	1958	1958	1958	2610	2610	2610	2610
R	0.699	0.658	0.713	0.707	0.794	0.826	0.829	0.821
RMSE	0.238	0.305	0.225	0.223	0.278	0.233	0.269	0.279
MBE	-0.098	0.130	0.041	0.015	-0.135	-0.055	-0.145	-0.158
GCOS	25.6	25.6	27.3	26.5	26.8	34.1	29.0	27.5

15